



OPEN

Enhanced Cold Field Emission of Large-area Arrays of Vertically Aligned ZnO-nanotapers via Sharpening: Experiment and Theory

Zhuo Zhang¹, Guowen Meng^{1,2}, Qiang Wu³, Zheng Hu³, Jingkun Chen⁴, Qiaoling Xu¹ & Fei Zhou¹

¹Key Laboratory of Materials Physics, and Anhui Key Laboratory of Nanomaterials and Nanostructures, Institute of Solid State Physics, Chinese Academy of Sciences, Hefei 230031, People's Republic of China, ²University of Science and Technology of China, Hefei 230026, People's Republic of China, ³Key Laboratory of Mesoscopic Chemistry of MOE, School of Chemistry and Chemical Engineering, Nanjing University, Nanjing 210093, People's Republic of China, ⁴State Key Laboratory of Optoelectronic Materials and Technologies, School of Physics and Engineering, Sun Yat-Sen University, Guangzhou 510275, People's Republic of China.

Large-area arrays of vertically aligned ZnO-nanotapers with tailored taper angle and height are electrodeposited on planar Zn-plate via continuously tuning the $\text{Zn}(\text{NH}_3)_4(\text{NO}_3)_2$ concentration in the electrolyte. Experimental measurements reveal that the field-emission performance of the ZnO-nanotaper arrays is enhanced with the sharpness and height of the ZnO-nanotapers. Theoretically, the ZnO-nanotaper is simplified to a “charge disc” model, based on which the characteristic macroscopic field enhancement factor (γ_C) is quantified. The theoretically calculated γ_C values are in good agreement with the experimental ones measured from arrays of ZnO-nanotapers with a series of geometrical parameters. The ZnO-nanotaper arrays have promising potentials in field-emission. The electrochemical synthetic strategy we developed may be extended to nanotaper arrays of other materials that are amenable to electrodeposition, and the “charge disc” model can be used for quasi-one-dimensional field emitters of other materials with nano-sized diameters.

Cold Electron Field Emission (CFE), rather than thermionic, photoelectric, or secondary emission, is a process in which electrons below or close to the emitter Fermi level escape from the emitter surface with the aid of a high electric field depressing the surface barrier at low temperature¹. One-dimensional (1D) field emitters with nano-sized diameters, such as nanowires^{2–4}, nanorods⁵ and nanotubes^{6–8}, have demonstrated higher emission efficiency than those with micro-sized diameters or film field emitters. In comparison, nanotapers^{9–12} have drawn much attention due to their larger characteristic macroscopic field enhancement factor (γ_C) and powerful ability to gather electrons on the top-tip. From the material view point, zinc oxide (ZnO) is very suitable for field emission owing to its thermal stability and oxide resistibility¹³. To date, randomly distributed cluster-like ZnO nanocones have been achieved on Zn-plate via hydro-thermal method¹⁴, and individual ZnO nanocones dispersed in solution have been synthesized via sol-gel reaction¹⁵. However these ZnO nanocones are not suitable for field emitters as they were not grown erectly on planar conducting substrates. Although, ZnO vertical nanotaper arrays were fabricated on Si substrates by thermal evaporation¹⁶, however, there was very limited control over the sharpness of the ZnO-nanotapers that has great effect on the field emission performance. Here we aim at large-area arrays of vertically aligned and parallel ZnO-nanotapers with well-controlled sharpness and height grown on planar conductive substrate to achieve much better field emission performance. Previously we electrodeposited arrays of vertically aligned hexagonal-shaped ZnO-nanorods with a uniform diameter from the bottom to the top-end on Si wafer by using Zn-sheet as the anode in $\text{Zn}(\text{NH}_3)_4(\text{NO}_3)_2$ electrolyte⁵, and the diameters of the ZnO-nanorods are approximately proportional to the $\text{Zn}(\text{NH}_3)_4^{2+}$ concentration in the electrolyte. In that case, the Zn-sheet anode was continuously electrolyzed into the electrolyte to form Zn^{2+} ions with the electrodeposition going on, leading to a constant Zn^{2+} concentration in the electrolyte during the whole electrodeposition process, thus every ZnO-nanorod has a uniform diameter from the bottom to the top-end. Herein, in order to grow ZnO-nanotapers on conductive substrate, we substitute graphite plate for Zn-sheet as the anode, and replace the Si wafer with Zn-plate substrate to achieve better lattice match for the ZnO-nanotapers and

SUBJECT AREAS:
NANOSCIENCE AND
TECHNOLOGY
THEORY AND COMPUTATION

Received
11 November 2013

Accepted
28 March 2014

Published
14 April 2014

Correspondence and
requests for materials
should be addressed to
G.W.M. (gwmeng@
issp.ac.cn)



better conductivity for field emission measurements. In the new set-up (see Supplementary Fig. S1), there is no any additional supplement of Zn^{2+} ions during the electrodeposition, the $\text{Zn}(\text{NH}_3)_4^{2+}$ concentration in the electrolyte decreases with the electrodeposition going on, thus arrays of ZnO-nanotapers (with their diameter decrease from the bottom to the top-end) rather than uniform-nanorods (with the same diameter from the bottom to the top-end) are electrodeposited on the Zn-plate substrate, and more importantly the taper angle (or sharpness) of the ZnO-nanotapers can be well-tailored via diluting the electrolyte during the electrodeposition.

Results

Top- (Fig. 1a) and side-view (Fig. 1b) scanning electron microscope (SEM) observations show large-area arrays of vertically aligned ZnO-nanotapers electrodeposited on the conductive Zn-plate. A close-up view (inset of Fig. 1a) displays the hexagonal cross-section of the resultant ZnO-nanotapers. A typical transmission electron microscope (TEM) image of a single ZnO-nanotaper (Fig. 1c) reveals that the diameter of the nanotaper decreases from the bottom to the top-end. Selected area electron diffraction (SAED) pattern (inset of Fig. 1c) taken from this nanotaper displays the single-crystal nature of the ZnO-nanotaper. The lattice-resolved TEM image (Fig. 1d) reveals the lattice fringes with a spacing of 0.26 nm, indicating that the ZnO-nanotaper grows along [0001] direction. Experimental measurements on CFE macroscopic current density (J_M) with the macroscopic field (F_M) (Fig. 1e) demonstrate that the arrays of the ZnO-nanotapers exhibit a larger CFE current density than that of the arrays of the ZnO-nanorods with the same height and the same bottom-diameter, where the measured current density is obtained at the emitter/vacuum interface. Based on the improvement on the Fowler-Nordheim (F-N) theory¹⁷, the “technically complete” FN-type equation is:

$$J_M = \alpha_M \lambda_C a \varphi^{-1} (\gamma_C F_M)^2 \exp(-v_F b \varphi^{3/2} / \gamma_C F_M), \quad (1)$$

where a and b are the first and second F-N constants respectively, v_F is a correction factor associated with barrier shape, and λ_C is a characteristic “supply correction factor”. α_M is the area efficiency of emission and is very much less than unity. The correction factor with

the largest influence on J_M is normally the barrier shape correction factor v_F . φ is the work function of the emitting material and γ_C is the characteristic enhancement factor, which is the ratio of the characteristic barrier field (F_C) over the F_M , and quantifies the emission ability of the emitter. The relationship between the slope of the F-N plot (S_M) and γ_C is $S_M = \frac{\partial \ln(J_M/F_M^2)}{\partial (1/F_M)} = -\frac{v_F b \varphi^{3/2}}{\gamma_C}$. The slope of the F-N plots is proportional to $-\varphi^{3/2}/\gamma_C$, where the F-N plots of $\ln(J_M/F_M^2)$ vs $1/F_M$, are shown in the inset of Fig. 1e, revealing that the arrays of ZnO-nanotapers have larger γ_C values and exhibit better CFE performance than those of the ZnO-nanorods with the same height and the same bottom-diameter.

To explore the effect of the nanotaper sharpness on the CFE performance of the ZnO-nanotaper arrays, we firstly tried to establish theoretical model and prepare a series of arrays of ZnO-nanotapers with different sharpness degrees, and then measure their CFE properties and further check the theoretical model. As for the theoretical models of field emission, most of the models have been established for carbon nanotubes (such as floating spheres¹⁸ and cylinders¹⁹) and metallic nanostructures (such as pyramids²⁰, hemi-ellipsoidal²¹ and semi-infinite electrodes²²). However, little has been reported on the semiconducting nano-emitters due to the complication mainly induced by the electric field penetration into the emitters and the surface states^{23–25}. For the field emitters consisting of metal and semiconductor, the emission ability is quantified by the γ_C value, which could be derived via numerical calculations (e.g., solving Laplace equation^{23,26}). However, numerical calculations involve complex formula derivation and require special software packages or computational programs. To simplify the calculation, a “floated sphere” model, which was first proposed by Miller in 1967 for the calculation of the “field intensification factor” of a single cylindrical field-emitter in small gaps²⁷, was employed to estimate the γ_C value of a single carbon nanotube¹⁸, and the making use of superposing the electrostatic potential of the “floated sphere” and that of its image simplifies the calculations to some extent. However, the double integral used in the spherical coordinate system is still complicated.

Here, we tried to establish a simple phenomenological “disc model” to calculate γ_C value of the semiconducting ZnO-nanotapers merely by single variable calculus in a circle plane system. Firstly, we

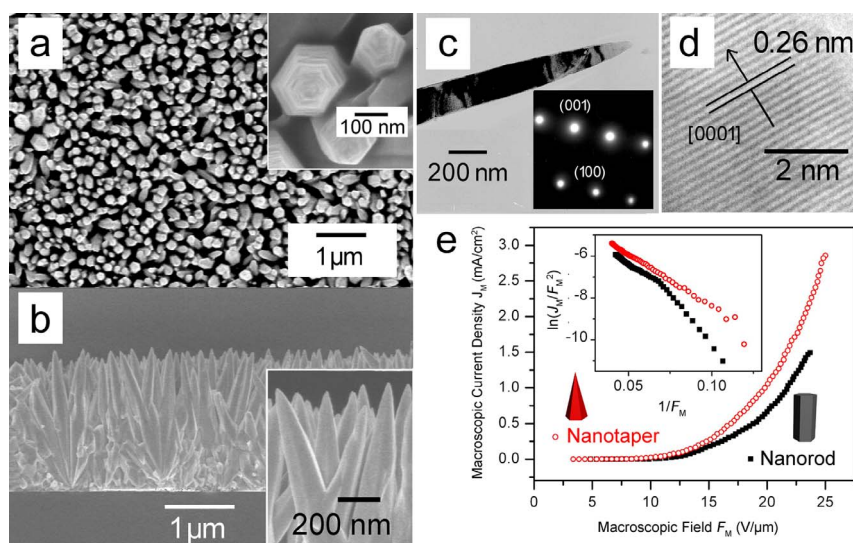


Figure 1 | ZnO-nanotaper arrays electrodeposited on Zn-plate in an initial 0.2 M $\text{Zn}(\text{NH}_3)_4^{2+}$ electrolyte with continuously injecting deionized (DI) water at 0.05 mL/min. (a), (b), Top- (a) and side-view (b) SEM images of the ZnO-nanotaper arrays (the insets are the close-up views). (c), TEM image of a single nanotaper (the inset is the SAED pattern). (d), Lattice-resolved TEM image taken on the nanotaper shown in (c). (e), Macroscopical current density (J_M) as a function of the applied electric field (F_M) for the arrays of ZnO-nanotapers with apical angle (θ) of 15° (red circles) and the ZnO-nanorods with the same bottom diameter of ~200 nm and the same height of ~2 μm (black squares). The insets are the corresponding F-N plots displayed with $\ln(J_M/F_M^2)$ and $1/F_M$.



model the hexagonal pyramid nanotaper as a nanocone with the same height and bottom area (Fig. 2a). Since the bottom radius of the nanocone (R_0) is very close to that of the circle (R_{ZnO}) inscribed the bottom of the ZnO-nanotaper: $R_0 = (2\sqrt{3}/\pi)^{1/2} \cdot R_{ZnO} \approx 1.05R_{ZnO}$. Then, the simplified nanocone with a height of h and a bottom radius of R_0 ($R_0 \ll h$) vertically standing on the cathode plate is put into a uniform electric field F_0 (Fig. 2b), with the distance between the anode and the cathode being D ($h \ll D$). Considering that the real top-tip of the ZnO-nanotaper is approximately a curved surface, therefore the top surface of the nanocone is simplified as a half sphere with a radius of r_1 tangent to the side of the nanocone. It is known that electrons are mainly emitted from the top-surface of the emitter, and the more the surface charges collected on the top-surface, the more the emission current is generated^{28,29}. In order to investigate the charge distributions on the top-surface of the cone-shaped emitter, as shown in Fig. 2c, the emitter is approximated as a sphere with a diameter of 10 nm, tangent to the side-face of the cone with the height of 2 μm . By solving the Laplace equation with the aid of finite element analysis under the zero charge boundary condition, we find that the surface charge is mainly concentrated on the upper surface of the sphere with its density decrease rapidly from the top-tip to the bottom under a macroscopic electric field of 20 V/ μm , being similar to that for the point discharge on the tips of the carbon nanotubes³⁰. Thus, we only consider the top-tip of the nanocone with

a height being equal to the diameter of the top sphere ($2r_1$). Secondly, as the field emission is entirely determined by the surface charges of the emitter, the nanocone is further simplified as a “charge disc” merely consisting of a layer of charges rather than ZnO (Fig. 2d). The charge density σ_0 of the “charge disc” is equal to the surface charge density at the center of the nanocone top-tip. The “charge disc” is tangent to the bottom of the sphere, and the radius R of the “charge disc” is determined by the sharpness (θ) and the height (h) of the nanotaper as follows:

$$R = r_0 + \left(r_1 + r_0 \tan \frac{\theta}{2} \right) \tan \frac{\theta}{2} \quad (2)$$

$$= r_0 \left[1 + \frac{R_0 - r_0}{h} \cdot \frac{\sqrt{h^2 + (R_0 - r_0)^2}}{h} + \frac{(R_0 - r_0)^2}{h^2} \right].$$

When $r_0 = R_0$, the nanotaper transforms into a nanorod with uniform diameter from the bottom to the top-end, the emission is mainly from the top face. When $r_0 = 0$, the nanotaper is a perfect cone, with the electron density on the surface of the top-tip being infinity ideally.

Due to the image force^{31,32} and for the satisfaction of the boundary condition that the “charge disc” and cathode are equipotential bodies, an equal image “charge disc” is put on the opposite side of the cathode (Fig. 2e)¹⁸. The potential of the “charge disc” is zero as

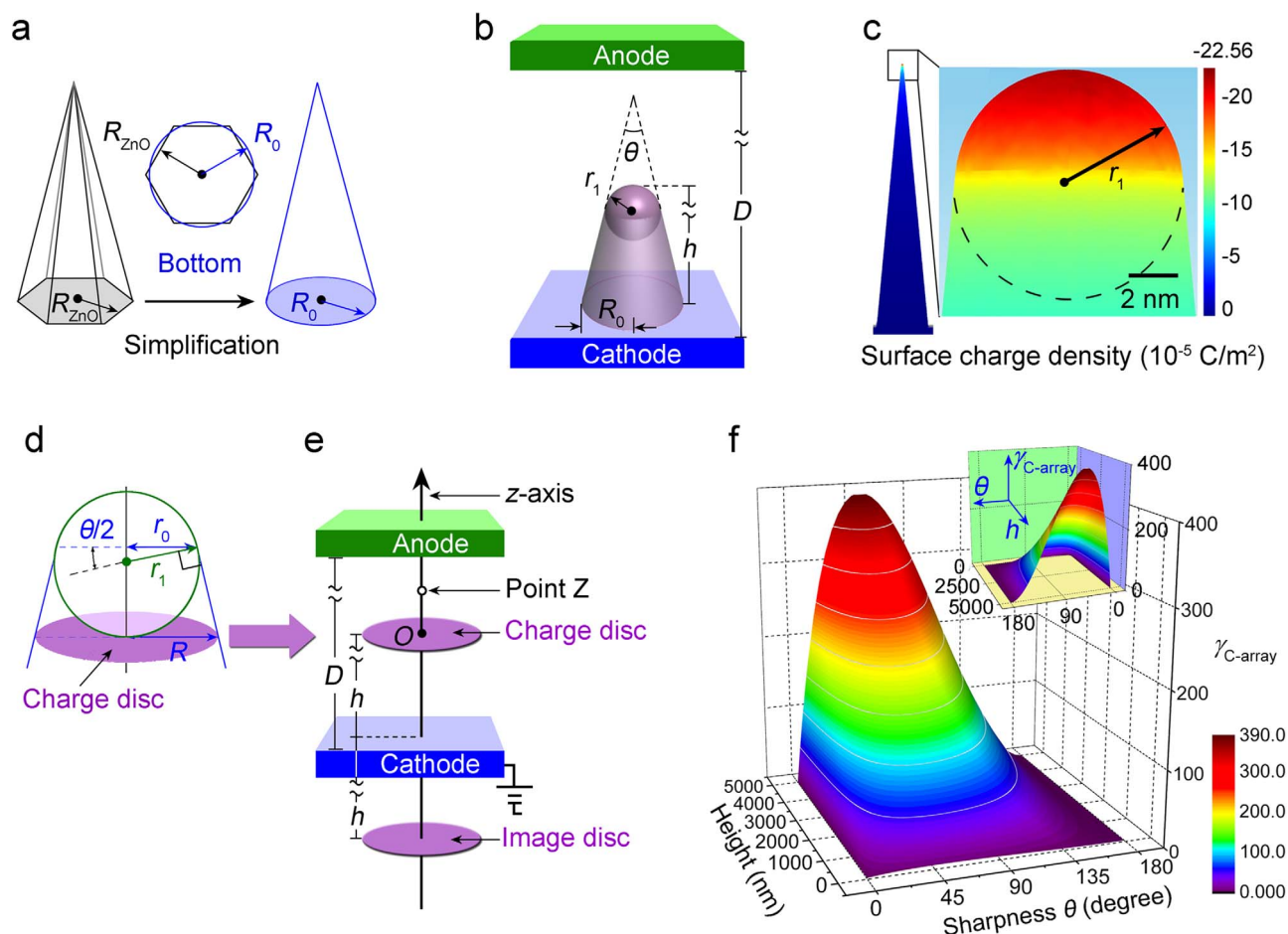


Figure 2 | Sketch for the modeling process and the solution of the “charge disc” model. (a), The hexagonal pyramid-shaped ZnO-nanotaper (left) is simplified into a cone-shaped nanotaper (right). (b), The simplified cone with a rounding-top in a uniform electric field F_0 . (c), The surface charge density distribution of the nanotaper ($h = 2 \mu\text{m}$, $R_0 = 200 \text{ nm}$) under the applied field $20 \text{ V}/\mu\text{m}$. (d), The disc radius R is determined by the top radius r_0 and the bottom radius R_0 of the ZnO-nanotaper. (e), The constructed charge disc (above the cathode) and image charge disc (below the cathode) model on the opposite side of the cathode. (f), Three-dimensional (3D) surface plot for the relationship among θ , h and $\gamma_{C\text{-array}}$ of the ZnO-nanotaper arrays, for clarity the inset is the back view of the diagram.



the cathode is connected to the ground. The potential ψ_z at point Z , above the center O of the “charge disc”, is composed of three parts as shown below:

$$\begin{aligned}\psi_z &= \psi_1 + \psi_2 + \psi_0 \\ &= \frac{1}{4\pi\epsilon_0} \int_0^R \frac{2\pi r \sigma_0 dr}{\sqrt{(z-h)^2 + r^2}} \\ &\quad - \frac{1}{4\pi\epsilon_0} \int_0^R \frac{2\pi r \sigma_0 dr}{\sqrt{(z+h)^2 + r^2}} + F_0 z \\ &= \frac{\sigma_0}{2\epsilon_0} (\sqrt{(z-h)^2 + R^2} - |z-h|) \\ &\quad - \frac{\sigma_0}{2\epsilon_0} (\sqrt{(z+h)^2 + R^2} - |z+h|) + F_0 z.\end{aligned}\quad (3)$$

Where ψ_1 , ψ_2 and ψ_0 are the potentials produced by disc charges, image disc charges and the applied field F_0 , respectively. When $z = h$ and $h \gg R$, the potential $\psi_{z=h} = \sigma_0 R / 2\epsilon_0 + F_0 h = 0$. So $\sigma_0 = 2\epsilon_0 F_0 h / R$, and the applied field on the surface ($z = h$) of the “charge disc” is

$$F_{disc,z=h} = \left. \frac{d\psi_z}{dz} \right|_{z=h} = \left| F_0 - \frac{\sigma_0}{2\epsilon_0} \right| = F_0 \left(\frac{h}{R} - 1 \right). \quad (4)$$

Thus, the characteristic field enhancement factor γ_{C-disc} of the “charge disc” is

$$\gamma_{C-disc} = F_{disc,z=h} / F_0 \approx h / R. \quad (5)$$

The results show that γ_{C-disc} is equal to h/R , being similar to that for nanorod³³ or nanotube³⁴. It should be mentioned that R is a function of the top radius r_0 and the sharpness θ of the nanotaper in our case.

Next, to get γ_C value of the ZnO-nanotapers, it is necessary to know the intrinsic characteristics of ZnO under the applied electric field. It has been reported that if an electric field is applied on a semiconducting emitter, the characteristics of the emitter will be changed due to the penetration of the applied electric field into the emitter²⁵ and the surface state³⁵. Specifically when the applied electric field penetrates from the surface into the emitter, much more extra electrons will appear on the top surface of the emitter. Then, the conduction band of ZnO has to bend downwards to supply enough holes for accommodating the extra electrons, as shown in Supplementary Fig. S2. Therefore, the characteristics of ZnO under the applied electric field depend on the degree of the band bending, and we have to estimate the magnitude of surface electronic density (σ) caused by the applied field at first, and then calculate the band bending at room temperature.

Under the applied external electric field F_0 , σ and the potential energy ϕ satisfy $\frac{d\phi}{dz} = -\frac{e}{\epsilon} F_s = -\frac{e}{\epsilon} (F_0 + \frac{4\pi\sigma}{\epsilon_0})$ ³⁶, where F_s is the total field and depends on the total electrons, and $\sigma = \epsilon_0(F_s - F_0) / 4\pi$. Under a commonly given external field of 20 V/ μm , if the band is not bent, the γ_C values deduced by putting the Electron Affinity and the work function into the F-N curve respectively are all close to 200. The identification whether the ϕ of ZnO is work function or Electron Affinity is illustrated in Supplementary Part 3. So,

$$\begin{aligned}\sigma < \epsilon_0 E_s / 4\pi = \epsilon_0 \gamma_C F_0 / 4\pi = 2.8144 \times 10^{-7} \\ \text{C/cm}^2 = 1.76 \times 10^{12} \text{ electrons/cm}^2.\end{aligned}\quad (6)$$

Then, we calculate the surface electronic density of ZnO with no band bending. In this case, the conduction band could accommodate all the extra electrons and the valence band is neglected. For ZnO, the density of states in the conduction band is

$$g_c(E) = 4\pi V \frac{(2m_n^*)^{3/2}}{h^3} (E - E_c)^{1/2}, \quad (7)$$

where V is the volume, E is the total energy, E_c is the energy level at the bottom of the conduction band, and m_n^* is the effective mass³⁶. The energy of electrons (E) follows the Fermi-Dirac distribution $f(E) = 1 / \{1 + \exp[(E - E_F) / (k_b T)]\}$, which is only related to the difference between the bottom of the conduction band and the Fermi level. Where E_F is the Fermi Level, k_b is the Boltzmann constant, and $T = 300$ K. So, the quantities of the electrons in the conduction band can be expressed as

$$\begin{aligned}N &= \int_{E_c}^{\infty} g_c(E) f(E) dE \\ &= \int_{E_c}^{\infty} 4\pi V \frac{(2m_n^*)^{3/2}}{h^3} (E - E_c)^{1/2} / [1 + \exp(\frac{E - E_F}{k_b T})] dE.\end{aligned}\quad (8)$$

Thus, the electronic density is

$$n = \frac{N}{V} = \int_{E_c}^{\infty} 4\pi \frac{(2m_n^*)^{3/2}}{h^3} (E - E_c)^{1/2} / [1 + \exp(\frac{E - E_F}{k_b T})] dE. \quad (9)$$

By numerical integration, we find that the electronic density of ZnO in the conduction band with no band bending is 3.85×10^{14} electrons/cm³. Assuming that the surface of ZnO is the outermost layer constructed with the Primitive Cells with a height of 5.2 Å³⁷, thus $\sigma = 2 \times 10^7$ electrons/cm², which is far less than the surface electron density when considering the band bending. So, when the band is bent, the surface charges are almost contributed with the electrons in the conduction band. From Eq. (9), the charge density n is proportional to $\exp[-(E_c - E_F) / k_b T]$. Therefore, when all the extra electrons are filled in the conduction band, the band bending is about 0.12 eV below the Fermi Level approximately. When considering the F_s and using self-consistent numeration, the order of magnitude of the σ for Ge is 10^{12} electron/cm² under the applied field of 0.3 V/Å³⁸. Similarly, the σ of ZnO has the same order of magnitude and is the difference between the surface electronic density with the band bending and that with no band bending. Because the surface electronic density with the band bending is much higher than that with no band bending, and the electronic density with no band bending is negligible. Thus, if the F_s is taken into account and all the extra electrons are filled in the conduction band, the band bending is about 0.12 eV below the Fermi Level. Based on the above analysis, if the F_s and all the extra electrons are filled in not only the conduction band but also the valence band, the band bending is also about 0.12 eV. This value makes the bottom of the conduction band below the Fermi Level with the magnitude of 10^{-1} eV. Compared with $k_b T = 0.026$ eV at room temperature (27°C), this magnitude of 10^{-1} eV is enough for semiconductor ZnO to have metallic properties.

After the analysis of the band bending caused by the field penetration, the effects of the surface states should be taken into account. The electrons emitted from semiconductors come from the following three parts: the conduction band, the valence band and the surface states²⁵. Since ZnO has a wide direct band gap and exhibits metallic properties, almost the entire electrons are emitted from the conduction band. Therefore, the formula for calculating the γ_C value of a single ZnO nanotaper is still Eq. (5), and the work function of ZnO is the difference between the vacuum level and the Fermi surface

$$\phi = |E_{c-nb} - E_F| + \chi = 0.24\text{eV} + 3.6\text{eV} = 3.84\text{eV}, \quad (10)$$

where E_{c-nb} is the vacuum level in conditions of no band bending, and χ is the Electron Affinity (see Supplementary Fig. S4). This result is similar to the work function of ZnO about 3.7 eV reported by K. Jacobi³⁹.

Considering that the shielding effect makes γ_C of the ZnO-nanotaper arrays ($\gamma_{C-array}$) lower than that of single nanotaper, the Eq. (5) is modified as follows



$$\gamma_{C-array} = (h/R) \cdot [1 - \exp(-1.1586d/h)]. \quad (11)$$

^{40,41}Where d is the gap distance between the nanotapers that really emit electrons. Then, by combining the Eq. (2) and (11), it can be seen that the $\gamma_{C-array}$ of the ZnO-nanotaper arrays is determined by both the height and the sharpness of the ZnO-nanotapers (Fig. 2f). With the height increase of the ZnO-nanotaper, the $\gamma_{C-array}$ increases owing to the continual rise of height-diameter ratio; with the increase of ZnO-nanotaper sharpness degree (apical angle θ , defined to quantitatively describe the sharpness) from 0° to 180° , the $\gamma_{C-array}$ increases rapidly at first and then slowly decreases since the shielding effect is dominated when the nanotapers are very sharp. It is important to note that the bottoms of the nanotapers are closely contacted with each other.

To test and verify the “disc model” and Eq. (11), experimental validations are performed. Firstly, we synthesized various arrays of ZnO-nanotapers with different θ and height-diameter ratios (h/R). By purposely dropping DI-water into the electrolyte to dilute the $Zn(NH_3)_4^{2+}$ concentration during the electrodeposition of ZnO-nanotaper arrays, the sharpness of the ZnO-nanotapers can be tailored. Without injecting DI-water, when the initial $Zn(NH_3)_4^{2+}$ concentration is 0.1 M, the θ of the resultant ZnO-nanotapers is $\sim 10^\circ$ (Fig. 3a). When DI-water is injected with a flow rate of 0.05, 0.1 and 0.2 mL/min, and the initial electrolyte concentration is kept at 0.2 M, nanotapers with θ of $\sim 15^\circ$, $\sim 25^\circ$ and $\sim 35^\circ$ are obtained respectively (Fig. 3b–d). The ZnO-nanotapers with the same bottom diameter (~ 100 nm) and different lengths can be achieved by tuning the electrodeposition duration and the initial volume of the electrolyte with the same initial concentration (see Supplementary Fig. S5).

The experimental J_M - F_M curves in Fig. 4(a) exhibit that the turn-on fields of the arrays of ZnO-nanotapers with θ of 10° , 15° , 25° and 35° are about 9.30, 9.90, 10.64 and 11.30 V/ μ m, respectively. Under an external field of about 20 V/ μ m, the current densities of these ZnO-nanotaper arrays are about 1.54, 1.20, 0.85 and 0.50 mA/cm², respectively. For getting the experimental $\gamma_{C-array}$ of the ZnO-nanotaper arrays from their J_M - F_M curves, it is essential to confirm the shape of CFE barrier and the slope of the F-N plots. Generally, the barrier shape of CFE is simplified as an elementary triangular. Then, $\alpha_M = \lambda_C = \nu_F = 1$ in Eq. (1), and $S_M = -b\phi^{3/2}/\gamma_C$. So, ν_F in Eq. (1) is not taken into account, which is an important factor for estimating

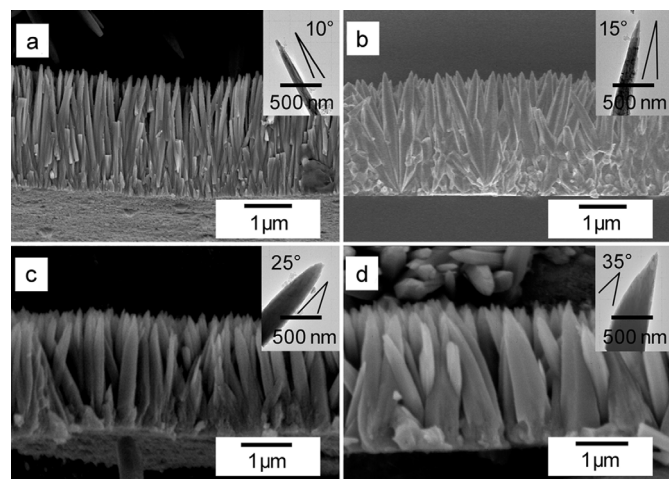


Figure 3 | Arrays of ZnO-nanotapers with the same height and different sharpness degrees. (a), Arrays of ZnO-nanotapers with the apical angle of $\sim 10^\circ$, achieved from initial 0.1 M $Zn(NH_3)_4^{2+}$ solution without injection of DI water. (b–d), Arrays of ZnO-nanotapers with apical angles of (b) 15° , (c) 25° and (d) 35° respectively, achieved from initial 0.2 M $Zn(NH_3)_4^{2+}$ solution by injecting the DI water with flow speed of 0.05, 0.1 and 0.2 mL/min, respectively. The insets are the TEM images.

γ_C ⁴². Considering that the tip of ZnO-nanotaper is modeled as a metallic “charge disc”, as we discussed above, the Schottky–Nordheim (S-N) barrier is more appropriate for us to estimate the experimental γ_C values. In this case, using the Forbes approximation⁴², $\nu_F \approx 1 - \frac{\gamma_C F_M}{F_h} + \frac{1}{6} \frac{\gamma_C F_M}{F_h} \ln \frac{\gamma_C F_M}{F_h}$. F_h is the field that could

reduce S-N barrier height from h to zero, and $F_h = \phi^2 / (\frac{K-1}{K+1} \frac{e^3}{4\pi\epsilon_0})$,

where K is the relative permittivity of ZnO and $K \approx 71$ ⁴³. If $\phi = 3.84$ eV and S_M is taken from the F-N plots shown in the inset of Fig. 4(a), the experimental $\gamma_{C-array}$ of the ZnO-nanotapers with θ of 10° , 15° , 25° and 35° are estimated to be 287, 280, 246 and 226, respectively, revealing that the sharper the ZnO-nanotaper is, the higher the F-E current is. Similarly, by using J_M - F_M curves and corresponding F-N plots of the ZnO-nanotapers with different heights under the same bottom diameters (~ 100 nm) (see Supplementary Fig. S6), the experimental $\gamma_{C-array}$ of the ZnO-nanotapers with heights of 1100, 1580, 2000 and 2620 nm are estimated to be 236, 280, 288 and 304, respectively.

Secondly, unlike the theoretical model that every nanotaper has effective emission, in practice only the highest or near the highest nanotapers can emit electrons. Besides, as the bottoms of the as-grown ZnO-nanotapers are contacted with each other, d increases inevitably with the sharpening of the ZnO-nanotapers. Thus, the d in Eq. (5) is corrected as $d = 2R_0[1 + 13.27 \exp(-0.07\theta)]$ via the non-linear fitting. (see Supplementary Fig. S7). Thirdly, it can be seen from Fig. S5 that the sharpness θ of our synthesized ZnO-nanotapers almost keeps a constant angle of about 5° when $h \geq 2000$ nm. Thus, Eq. (11) is finally determined as:

$$\gamma_{C-array} = \begin{cases} (h/R)[1 - \exp(-1.1586d/h)], & \text{when } h < 2000\text{nm, or } \theta > 5^\circ \\ (h/R)[1 - \exp(-1.1586 \times 2000d/h^2)], & \text{when } h \geq 2000\text{nm and } \theta \leq 5^\circ \end{cases} \quad (12)$$

Based on Eq. (12), the theoretical 3D-surface for $\gamma_{C-array}$ is shown in Fig. 4b, revealing that $\gamma_{C-array}$ has three regions with the increase of θ : rapid rising region (I, $0^\circ < \theta < 16^\circ$), rapid dropping region (II, $16^\circ < \theta < 60^\circ$) and slow dropping region (III, $\theta > 60^\circ$). From $\theta = 0^\circ$ to $\theta = 60^\circ$, both the shielding effect and the enhanced emission are weakened gradually with the sharpness decrease of the ZnO-nanotapers. When $0^\circ < \theta < 16^\circ$, the shielding effect is stronger and dominant; when $\theta \approx 16^\circ$, the shielding effect and the emission are nearly balanced; when $16^\circ < \theta < 60^\circ$, the shielding effect is relatively weaker and decreases faster than that of the emission; when $\theta > 60^\circ$, the shielding effect almost disappears and the emission decreases slowly. The difference for the theoretical $\gamma_{C-array}$ before and after the correction of d (Fig. 4c) firstly increases rapidly and then increases slowly with h ; and the positive and negative maximal differences center at $\theta \approx 16^\circ$ and $\theta \approx 60^\circ$, respectively. It clearly demonstrates that with the increase of h the shielding effect increases rapidly at first, and then slows down gradually; at $\theta \approx 16^\circ$, the shielding effect and the emission are indeed nearly balanced; at $\theta \approx 60^\circ$, the shielding effect just disappears. Fourthly, the sparsity effect of emitters is very important to the CFE performance. By using Eq. (12), we find that $\gamma_{C-array}$ of the ZnO-nanotapers increases with the distance between the adjacent ZnO-nanotapers (d_a) until $\gamma_{C-array} = \gamma_C$ (see Supplementary Fig. S8). It reconfirms that the shielding effect weakens gradually with the increase of d_a and diminishes finally when d_a is large enough. For our ZnO-nanotapers, $d_a = 0$. So, finally, the $\gamma_{C-array}$ calculated via the “charge disc” model and those deduced from the slope of the experimental F-N plots for the arrays of ZnO-nanotapers with different θ and h are shown in the upper and lower row of Fig. 4d, respectively. The theoretical result from the “charge disc” model is well confirmed by the experiments. The deviations may result from adsorbed gases, crystal defects and *etc.*⁴⁴

To test and verify the universality of our theoretical “charge disc” model for 1D field nanoemitters of various materials, we calculated the $\gamma_{C-array}$ of 1D field emitters of various materials with nano-sized

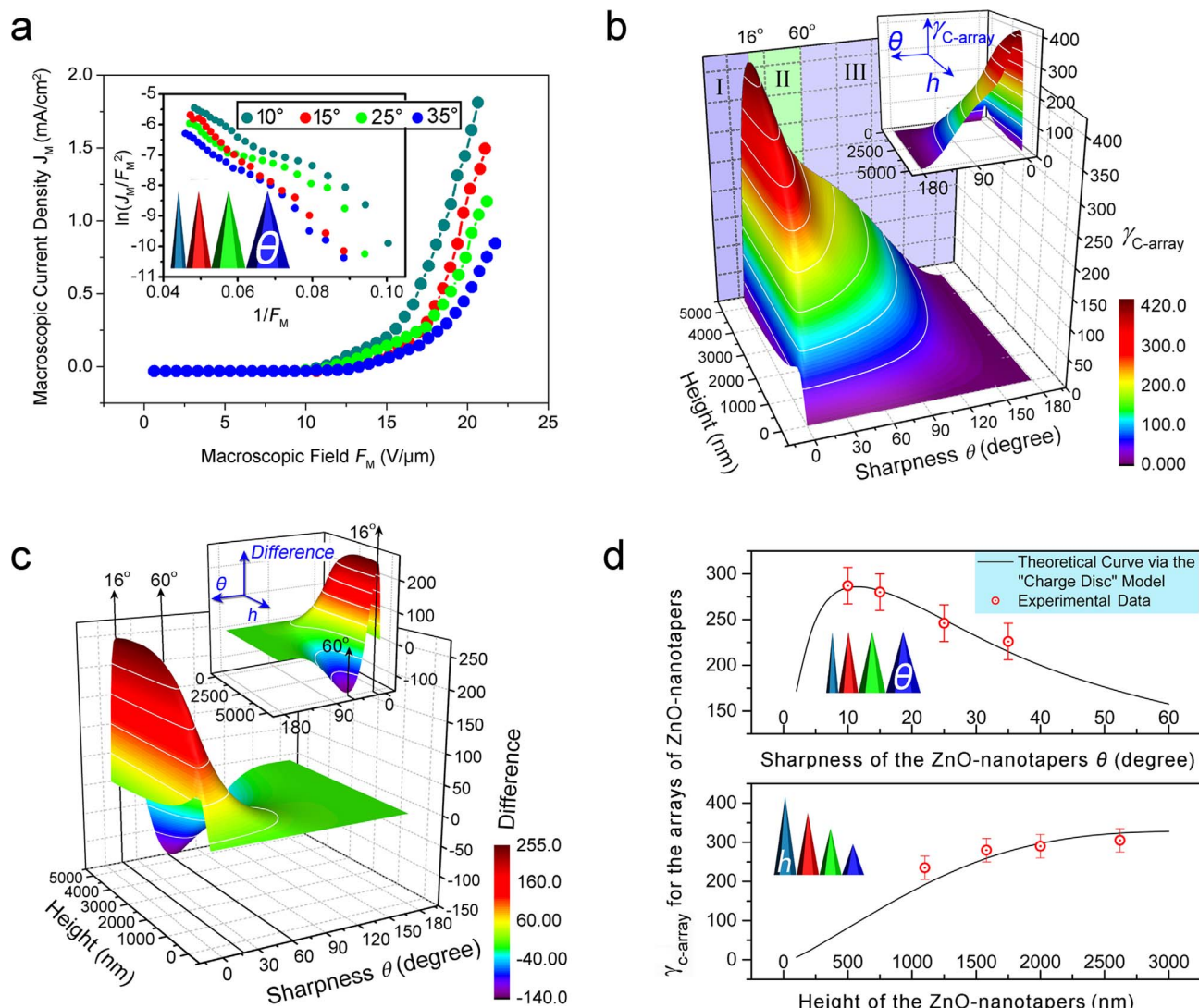


Figure 4 | Experimental verification of the “charge disc” mode. (a), J_M - F_M curves for the arrays of ZnO-nanotapers with the same h of 2 μm and different θ of 10°, 15°, 25° and 35° respectively. (b), 3D-surface for the relationship among θ , h and $\gamma_{C\text{-array}}$ of the ZnO-nanotaper arrays, where the three regions of I, II and III are marked respectively. For clarity, the inset is the back view. (c), The 3D-surface for the difference between the theoretical $\gamma_{C\text{-array}}$ values before and after the correction of d . The inset is the back view. (d), Comparison between the theoretical curves calculated from the “disc model” and the experimental data of $\gamma_{C\text{-array}}$ for the arrays of the ZnO-nanotapers with different θ (upper) and h (lower), respectively. Error bars show the deviation of experimental accuracy.

diameters reported previously in the literature, such as single carbon nanotube⁸, Cu nanocones⁴⁵, SiC nanocones⁹ and AlN nanocones¹², via our “charge disc” model (see Supplementary Fig. S9 and Table S1). Fortunately, the theoretical results agree well with the experimental values reported in the literature, further demonstrating that our “charge disc” model can also be applied to quasi-1D field emitters of other materials with nano-sized diameters.

Discussion

In summary, arrays of ZnO-nanotapers with well-tailored sharpness and height have been grown on Zn-plate via electrodeposition by using graphite as anode and tuning $\text{Zn}(\text{NH}_3)_4(\text{NO}_3)_2$ concentration in the electrolyte. The field emission performance of the resultant ZnO-nanotaper arrays has improved with the increase of the sharpness and the height of the ZnO-nanotapers. The synthetic approach may be exploited to arrays of nanotapers consisting of other materials that are amenable to electrodeposition. A “charge disc” model has been designed to calculate the γ_C of the ZnO-nanotaper and its arrays. The theoretically calculated γ_C values from the “charge disc”

model have similar tendency but a little bit higher than the experimental ones. The disc model can also be used for quasi-1D field emitters of other materials with nano-sized diameters to predict their field emission performance.

Methods

Experimental. Vertical aligned arrays of hexagonal ZnO-nanotapers were electrodeposited on Zn-sheet cathode in $\text{Zn}(\text{NH}_3)_4(\text{NO}_3)_2$ electrolyte in a Teflon cell with graphite as working electrode (see Fig. SM1). The electrochemical cell (with volume of 200 mL) was put into a water bath at 80 °C. The $\text{Zn}(\text{NH}_3)_4(\text{NO}_3)_2$ electrolyte was prepared by gradually dropping ammonium hydroxide (28 wt% NH_3 in water, 99.99%) into zinc nitrate hexahydrate [$\text{Zn}(\text{NO}_3)_2 \cdot 6\text{H}_2\text{O}$, 99.0%] aqueous solution till the solution became clear. To form ZnO-nanotapers, the electrolyte concentration is gradually decreased by injecting DI water into the solution with a flow controller.

Characterization. The ZnO-nanotapers were characterized by using field-emission SEM (SIRION 200), TEM (JEM-2010) and X-ray diffraction (XRD) (X'Pert Pro MPD). F-E properties were measured with a parallel-plate diode setup in a vacuum chamber under a pressure about 6×10^{-5} Pa at room temperature.

Simulation. The surface charge density of the simplified cone shown in Fig. 2c was calculated by using a finite-element simulation method.



- Murphy, E. L. & Good, Jr, R. H. Thermionic Emission, field Emission, and the transition Region. *Phys. Rev.* **102**, 1464–1473 (1956).
- Rinzler, A. G. *et al.* Unraveling nanotubes: field emission from an atomic wire. *Science* **269**, 1550–1553 (1995).
- Wang, X. D. *et al.* In situ field emission of density-controlled ZnO nanowire arrays. *Adv. Mater.* **19**, 1627–1631 (2007).
- She, J. C. *et al.* Correlation between resistance and field emission performance of individual ZnO one-dimensional nanostructures. *ACS Nano* **2**, 2015–2022 (2008).
- Zhang, Z. *et al.* Aligned ZnO nanorods with tunable size and field emission on native Si substrate achieved via simple electrodeposition. *J. Phys. Chem. C* **114**, 189–193 (2010).
- de Heer, W. A., Châtelain, A. & Ugarte, D. A carbon nanotube field-emission electron source. *Science* **270**, 1179–1180 (1995).
- Fan, S. S. *et al.* Self-oriented regular arrays of carbon nanotubes and their field emission properties. *Science* **283**, 512–514 (1999).
- Xu, Z., Bai, X. D., Wang, E. G. & Wang, Z. L. Field emission of individual carbon nanotube with in situ tip image and real work function. *Appl. Phys. Lett.* **87**, 163106 (2005).
- Huq, S. E., Prewett, P. D., She, J. C., Deng, S. Z. & Xu, N. S. Field emission from amorphous diamond coated silicon tips. *Mater. Sci. and Eng.* **B74**, 184–187 (2000).
- Zhang, Z. J., Zhao, Y. & Zhu, M. M. NiO films consisting of vertically aligned cone-shaped NiO rods. *Appl. Phys. Lett.* **88**, 033101 (2006).
- Machado, M., Piquini, P. & Mota, R. The influence of the tip structure and the electric field on BN nanocones. *Nanotech.* **16**, 302–306 (2005).
- Liu, F. *et al.* Controlled growth and field emission of vertically aligned AlN nanostructures with different morphologies. *Chin. Phys. B* **18**, 2016–2023 (2009).
- Zhang, H., Yang, D. R., Ma, X. Y. & Que, D. L. Synthesis and field emission characteristics of bilayered ZnO nanorod array prepared by chemical reaction. *J. Phys. Chem. B* **109**, 17055–17059 (2005).
- Du, G. H., Xu, F. Z., Yuan, Y. & Van Tendeloo, G. Flowerlike ZnO nanocones and nanowires: preparation, structure, and luminescence. *Appl. Phys. Lett.* **88**, 243101 (2006).
- Joo, J., Kwon, S. G., Yu, J. H. & Hyeon, T. Synthesis of ZnO nanocrystals with cone, hexagonal cone, and rod shapes via non-hydrolytic ester elimination sol-gel reactions. *Adv. Mater.* **17**, 1873–1877 (2005).
- Han, X. H. *et al.* Controllable synthesis and optical properties of novel ZnO cone arrays via vapor transport at low temperature. *J. Phys. Chem. B* **109**, 2733–2738 (2005).
- Forbes, R. G. Physics of generalized Fowler-Nordheim-type equations. *J. Vac. Sci. Technol. B* **26**, 788 (2008).
- Wang, X. Q., Wang, M., He, P. M., Xu, Y. B. & Li, Z. H. Model calculation for the field enhancement factor of carbon nanotube. *J. Appl. Phys.* **96**, 6752–6755 (2004).
- He, C. S., Wang, W. L., Deng, S. Z., Xu, N. S. & Li, Z. B. Anode distance effect on field electron emission from carbon nanotubes: a molecular/quantum mechanical simulation. *J. Phys. Chem. A* **113**, 7048–7053 (2009).
- de Assis, T. A., Borondo, F., de Castilho, C. M. C., Mota, F. B. & Benito, R. M. Field emission properties of an array of pyramidal structures. *J. Phys. D: Appl. Phys.* **42**, 195303 (2009).
- Pogorelov, E. G., Zhbanov, A. I. & Chang, Y. C. Field enhancement factor and field emission from a hemi-ellipsoidal metallic needle. *Ultramicroscopy* **109**, 373–378 (2009).
- Gohda, Y., Nakamura, Y., Watanabe, K. & Watanabe, S. Self-Consistent Density Functional Calculation of Field Emission Currents from Metals. *Phys. Rev. Lett.* **85**, 1750–1753 (2000).
- Alivova, Y. & Molloy, S. Calculation of field emission enhancement for TiO₂ nanotube arrays. *J. Appl. Phys.* **108**, 024303 (2010).
- Qu, C. Q. *et al.* First-principles density-functional calculations on the field emission properties of BN nanocones. *Solid State Comm.* **146**, 399–402 (2008).
- Stratton, R. Field Emission from Semiconductors. *Proc. Phys. Soc. B* **68**, 746–757 (1955).
- Young, R., Ward, J. & Scire, F. Observation of metal-vacuum-metal tunneling, field emission, and the transition region. *Phys. Rev. Lett.* **27**, 922–924 (1971).
- Miller, H. C. Change in field intensification factor β of an electrode projection (whisker) at short gap lengths. *J. Appl. Phys.* **38**, 4501 (1967).
- Pan, Z. W. *et al.* Oriented silicon carbide nanowires: synthesis and field emission properties. *Adv. Mater.* **12**, 1186–1190 (2000).
- Zheng, X., Chen, G. H., Li, Z. B., Deng, S. Z. & Xu, N. S. Quantum-mechanical investigation of field-emission mechanism of a micrometer-long single-walled carbon nanotube. *Phys. Rev. Lett.* **92**, 106803 (2004).
- Wang, Z. L., Gao, R. P., de Heer, W. A. & Poncharal, P. In situ imaging of field emission from individual carbon nanotubes and their structural damage. *Appl. Phys. Lett.* **80**, 856–858 (2002).
- Grahame, D. C. The electrical double layer and the theory of electrocapillarity. *Chem. Rev.* **41**, 441–501 (1947).
- Hart, A., Satyanarayana, B. S., Milne, W. I. & Robertson, J. Field emission from tetrahedral amorphous carbon as a function of surface treatment and substrate material. *Appl. Phys. Lett.* **74**, 1594 (1999).
- Edgcombe, C. J. & Valdré, U. J. Microscopy and computational modeling to elucidate the enhancement factor for field electron emitters. *J. Microsc.* **203**, 188–194 (2001).
- Wang, X. Q., Wang, M., Li, Z. H., Xu, Y. B. & He, P. M. Modeling and calculation of field emission enhancement factor for carbon nanotubes array. *Ultramicroscopy* **102**, 181–187 (2005).
- Forbes, R. G. Low-macroscopic-field electron emission from carbon films and other electrically nanostructured heterogeneous materials: hypotheses about emission mechanism. *Solid-State Electron.* **45**, 779–808 (2001).
- Modinos, A. Field, Thermionic and Secondary Electron Emission Spectroscopy (Plenum Press, New York, 1984).
- Özgür, Ü. *et al.* A comprehensive review of ZnO materials and devices. *J. Appl. Phys.* **98**, 041301 (2005).
- Shepherd, W. B. & Peria, W. T. Observation of surface-state emission in the energy distribution of electrons field-emitted from (100) oriented Ge. *Surf. Sci.* **38**, 461–498 (1973).
- Jacobi, K., Zwicker, G. & Gutmann, A. Work function, electron affinity and band bending of zinc oxide surfaces. *Surf. Sci.* **141**, 109–125 (1984).
- Nilsson, L. *et al.* Scanning field emission from patterned carbon nanotube films. *Appl. Phys. Lett.* **76**, 2071–2073 (2000).
- Bonard, J. M. *et al.* Tuning the field emission properties of patterned carbon nanotube films. *Adv. Mater.* **13**, 184–188 (2001).
- Forbes, R. G. & Deane, J. H. B. Reformulation of the standard theory of Fowler-Nordheim tunnelling and cold field electron emission. *Proc. R. Soc. A* **463**, 2907–2927 (2007).
- Gupta, M. K. *et al.* Piezoelectric, dielectric, optical and electrical characterization of solution grown flower-like ZnO nanocrystal. *Mater. Lett.* **63**, 1910–1913 (2009).
- Gadzuk, J. W. & Plummer, E. W. Field emission energy distribution (FEED). *Rev. Mod. Phys.* **45**, 487–548 (1973).
- Seribun, P. *et al.* Copper nanocones grown in polymer ion-track membranes as field emitters. *Eur. Phys. J. Appl. Phys.* **58**, 10402 (2012).

Acknowledgments

The work was supported by the National Key Basic Research Program of China (Grant 2013CB934304), the NSFC (Grants 11104267, 11274312 and 21207134) for the financial support.

Author contributions

Z.Z. and G.W.M. conceived the concepts of the research. Z.Z. designed and prepared samples, and set up models. Q.W. and Z.H. measured the field emissions of the samples. J.K.C. and F.Z. carried out the finite-element simulations. Z.Z., G.W.M. and Q.L.X. wrote the manuscript. All authors contributed to revising the manuscript.

Additional information

Supplementary information accompanies this paper at <http://www.nature.com/scientificreports>

Competing financial interests: The authors declare no competing financial interests.

How to cite this article: Zhang, Z. *et al.* Enhanced Cold Field Emission of Large-area Arrays of Vertically Aligned ZnO-nanotapers via Sharpening: Experiment and Theory. *Sci. Rep.* **4**, 4676; DOI:10.1038/srep04676 (2014).



This work is licensed under a Creative Commons Attribution-NonCommercial-NoDerivs 3.0 Unported License. The images in this article are included in the article's Creative Commons license, unless indicated otherwise in the image credit; if the image is not included under the Creative Commons license, users will need to obtain permission from the license holder in order to reproduce the image. To view a copy of this license, visit <http://creativecommons.org/licenses/by-nc-nd/3.0/>